Journal of the Ceramic Society of Japan 132 [5] 205-213 2024
DOI https://doi.org/10.2109/jcersj2.23096

JCS-Japan

FULL PAPER

Corrosion behavior of calcium-magnesium-alumino-silicate on $(La,Gd)_2Zr_2O_7$/YSZ multilayer for thermal barrier coatings

Seung-Hyeon Kim[1], Toshio Osada[1], Kee-Sung Lee[2], Yoon-Suk Oh[3], Nobuo Nagashima[1] and Byung-Koog Jang[4,†]

[1] Research Center for Structural Materials, National Institute for Materials Science, 1–2–1 Sengen, Tsukuba, Ibaraki 305–0047, Japan
[2] School of Mechanical Engineering, Kookmin University, Seoul 02707, Republic of Korea
[3] Korea Institute of Ceramic Engineering and Technology, 3321 Gyeongchung Rd., Sindun-Myeon, Icheon 17303, Republic of Korea
[4] Interdisciplinary Graduate School of Engineering Science, Kyushu University, 6–1 Kasuga-koen, Kasuga, Fukuoka 816–8580, Japan

In this study, the high-temperature corrosion behavior was evaluated for $(La,Gd)_2Zr_2O_7$ (LGZ) used as a promising thermal barrier coatings (TBCs) material. $(La,Gd)_2Zr_2O_7$ + YSZ multilayer prepared from atmospheric plasma spray (APS) were exposed to calcium-magnesium-alumino-silicate (CMAS) melt at 1300 °C for 2, 12, 48, and 100 h. Molten CMAS and $(La,Gd)_2Zr_2O_7$ reacted to form reaction layer $Ca_2Gd_8(SiO_4)_6O_2$ (apatite) at 1300 °C. The thickness of the reaction layer increased with increasing heat-treatment time. A correlation between the hardness and Young's modulus relationship for the reaction layer of the coating was observed for the microstructure using nanoindentation. It was confirmed that the pores of the coating were reduced through the infiltration of molten CMAS in the initial stage of the corrosion reaction, and the hardness and Young's modulus were increased due to densification. Fracture toughness increased with heat treatment time in both directions (in-plane and through-thickness). The fracture toughness in the in-plane direction is 0.19–0.23 MPa$\sqrt{m}$. On the other hand, the fracture resistance in the thickness direction was 0.87–1.26 MPa$\sqrt{m}$, which was higher than that in the in-plane direction. These results show that the crack propagates in the in-plane direction and causes TBC delamination.

Key-words : Thermal barrier coatings, Corrosion, CMAS, Rare-earth zirconate

[Received May 12, 2023; Accepted March 4, 2024]

1. Introduction

Gas turbines are used in various applications such as aircraft and generator turbine engines. It is well known that the higher the operating temperature, the higher the energy efficiency.[1),2)] Therefore, studies have been conducted related to increasing energy efficiency by increasing the operating temperature by applying thermal barrier coatings (TBCs). In order to increase the durability of TBCs, high melting point, low thermal conductivity, excellent thermal and chemical stability, no phase change, and excellent corrosion resistance or calcium-magnesium-alumino-silicate (CMAS) resistance are required. A typical TBC uses tetragonal partially stabilized zirconia (4 mol % Y_2O_3–ZrO_2, YSZ) stabilized by adding Y_2O_3 to a thickness of 100 µm to 1 mm. YSZ is commonly used in TBC systems due to its low coefficient of thermal conductivity and high coefficient of thermal expansion.[3),4)] Recently, volcanic eruptions have been actively occurring, and the volcanic ash generated is deposited on the high-temperature parts of turbine engines and deteriorates. Volcanic ash melted at high temperatures penetrates TBCs through pores and microcracks. As heating and cooling are repeated, mechanical stress is generated, which significantly reduces the life of high-temperature parts. As a result, metastable tetragonal (t′) YSZ decomposes into tetragonal (t) and cubic (c) phases. During cooling, it is transformed into a monoclinic phase (m) with excessive volume expansion, leading to cracking and failure of the coating.[5)] Therefore, many studies have been conducted on the high-temperature corrosion evaluation by artificially manufactured CMAS with components like volcanic ash.[6)–12)]

Therefore, new ceramic materials such as RE zirconate[13)–16)] have been proposed due to their excellent properties, such as lower thermal conductivity and better CMAS attack resistance as compared to YSZ.[17)] Therefore, to improve durability against CMAS, a double-layer TBC with YSZ as the middle layer and RE zirconate as the top ceramic layer has been proposed. In addition, electron beam–physical vapor deposition (EB–PVD) of the typical TBC coating method[18),19)] has the advantage of being resistant to more stains, so it is mainly applied to the most important parts exposed to harsh environments in aircraft engines, such as high-pressure turbine vanes and blades. To complement the EB–PVD method, an atmospheric plasma

† Corresponding author: B.-K. Jang; E-mail: jang.byungkoog@kyudai.jp

spray (APS) system is an alternative.[13),20),21)] Especially, the multilayer $Gd_2Zr_2O_7$ and ceria–yttria stabilized zirconia (CYSZ) TBC fabricated by APS.[13)] It is reported that the thermal cycling performance of the $Gd_2Zr_2O_7$ coating is improved thanks to the multilayer design.[13)] Developing APS coatings with unique microstructural features is shown to be an effective way to obtain multilayer microstructures. In the structure of the multilayer ceramic TBCs, the first ceramic layer is coated with YSZ, which has a relatively large thermal expansion coefficient and excellent mechanical properties,[22)] directly on the superalloy substrate and the bond coat. As the second ceramic layer is exposed to high temperatures, it is coated with rare earth zirconate, which has excellent high-temperature phase stability and can be applied at higher temperatures than existing YSZ TBCs. Like YSZ, new TBC materials should not exhibit phase transformation at high temperatures and should have very low sintering rates at temperatures of more than 1200 °C.

$Gd_2Zr_2O_7$ (GZO) has proven to be a promising TBC material with better CMAS corrosion resistance than YSZ. In recent years, Gd-zirconate[13)–15),17),22)–24)] TBCs and La-zirconate[16),21)] TBCs with relatively high thermal stability and relatively low thermal conductivity have been studied. The reason why La doped is that $La_2Zr_2O_7$ has a high melting point (2300 °C) and no phase transformation, so it maintains stability at high temperatures.[25)] It can also prevent molten CMAS corrosion by forming $Ca_2La_8(SiO_4)_6O_2$.[26)]

However, there are few reports regarding CMAS corrosion behavior for La-doped GZO, and the effect on CMAS corrosion resistance is still unclear. In addition, the hardness and Young's modulus of the reaction layer after high-temperature corrosion by CMAS are important characteristics in evaluating the durability of the coating layer. This study demonstrates that it provides both chemical and mechanical influences on high-temperature corrosion behavior. In order to evaluate the corrosion resistance of the $(La,Gd)_2Zr_2O_7$ (LGZ: lanthanum Gadolinium Zirconate), CMAS was applied to the surface of the coating layer, and heat treatment was performed at 1300 °C for 2 to 100 h. In this way, the high-temperature degradation behavior by CMAS was investigated through the analysis of the composition and microstructure of the $(La,Gd)_2Zr_2O_7$/YSZ multilayer coating according to the heat treatment time.

2. Experimental procedure

2.1 Preparation of $(La,Gd)_2Zr_2O_7$/YSZ multilayer coating

The powder for the TBC was made into a spherical shape by spray drying. This spherical powder was melted by plasma, and the top coating powder was thermal sprayed on the bond coating (AMDRY 386-2) at high temperature and high pressure. CMSX-4 (nickel-based superalloys) with a thickness of 3 mm was used as a substrate. The top was coated with Triplex APS (Triplex Pro-200, Oerlikon Metco). The top coating layer controls the size and distribution of the powder (making YSZ spheroidized powder with a size of 45–125 μm), and optimizes the gun distance, powder feed rate, and spray speed. The composition was mixed as ZrO_2:La_2O_3:Gd_2O_3 = 43.65:6.41:49.94 in weight ratio (The composition by molar ratio was formulated to be $La_{0.25}Gd_{1.75}Zr_2O_7$). As the top coating layer, a multilayer composed of three layers was prepared. Low thermal conductivity $(La,Gd)_2Zr_2O_7$ is on the top layer (250 um), and the bottom layer is dense YSZ (150 um). The middle layer (150 um) was composed of a mixture of LGZ and YSZ at a ratio of 1:1.

2.2 Microstructure and high-temperature corrosion

The CMAS powder used in the corrosion experiments was prepared using the same method as in our previous works.[6)–12)] The composition of CMAS is 33CaO–9MgO–13AlO1.5–45SiO_2 mol.%.[6),8)–10),12)] The $(La,Gd)_2Zr_2O_7$/YSZ multilayer coating was cut into 10 mm × 5 mm using a diamond saw. To evaluate the CMAS high-temperature corrosion behavior, a paste prepared by mixing the CMAS powder with ethanol ultrasonically was applied to the upper surface of $(La,Gd)_2Zr_2O_7$ coating in the amount of 40 mg/cm^2. Specimens were heated to 1300 °C using a heating rate of 10 °C/min and held for 2, 12, 48, or 100 h before being furnace cooled to room temperature. After heat treatment, specimens were cut into 5 mm × 5 mm, and their cross sections were polished successively using 9, 3, and 1 μm diamond suspensions to analyze the reaction layer.

The $(La,Gd)_2Zr_2O_7$/YSZ multilayer coating, together with the microstructural and compositional changes taking place, was analyzed after cooling using a scanning electron microscope (SEM; EISS Gemini SEM 300, Germany) with a beam voltage of 15 kV, and a working distance of 15 mm was used for energy-dispersive X-ray spectroscopy (EDS) measurements to determine the compositions of the specimen cross section. The evolution of the crystalline phases was tracked by performing X-ray diffraction (XRD) with Cu Kα radiation (λ = 1.54056 Å) using a Rigaku Smart Lab diffractometer (Rigaku Co., Japan) on either sintered compacts or powders. XRD measurements were taken at room temperature using a scan step of 0.02° and a scan rate of 1°/min in the 2θ range of 20–60°.

2.3 Mechanical properties

The values of Martens hardness (*HM*) and Young's modulus of the cross-section of the $(La,Gd)_2Zr_2O_7$/YSZ multilayer coating subjected to different thermal treatments were measured at room temperature using a nanoindentation testing system (DUH-2110, Shimadzu, Japan). A 115° triangular pyramid indenter was used at a constant load of 100 mN, with loading and unloading times of 5 s each. The Martens hardness was calculated using Eq. (1), where F is the maximum force and h is the depth of penetration at that force.[27)]

$$HM_{115} = 1000F/26.43 \times h^2 \quad (1)$$

The indentation elastic modulus (E_{it}) is considered equivalent to Young's modulus,[28)] which is analyzed with the same method as in our previous studies.[29)–33)] Where

Hv represents Vickers hardness and E and Young's modulus. $d_{//}$ and $d_{\perp}$ represent the diagonal lengths in the in-plane and through-the-thickness directions, respectively. a_l, a_r, a_u, and a_d are the crack lengths propagated from the left, right, top, and bottom edges, respectively. To evaluate fracture toughness (K_C) values for both in-plane and through-thickness directions were measured with the following Eq. (2):[34]

$$K_C = 0.071(H_V\sqrt{d})(E/H_V)^{2/5}(c/d)^{-3/2} \quad (2)$$

$$\left(c = c_{//} \text{ or } c_{\perp},\ d = \frac{d_{//} + d_{\perp}}{2}\right)$$

$$c_{//} = \frac{d_{//} + d_{\perp}}{4} + \frac{a_l + a_r}{2}$$

$$c_{\perp} = \frac{d_{//} + d_{\perp}}{4} + \frac{a_u + a_d}{2}$$

3. Results and discussion

3.1 Characterization of the $(La,Gd)_2Zr_2O_7$/YSZ multilayer coating

Figure 1 shows the XRD patterns of $(La,Gd)_2Zr_2O_7$/YSZ multilayer coatings (hereafter abbreviated to LGZ) from 0 to 100 h at 1300 °C. Figure 1(a) shows the XRD pattern before heat treatment. Figure 1 shows XRD patterns after heat treatment for (b) 2 h, (c) 12 h, (d) 48 h, and (e) 100 h. After heat treatment, peaks corresponding to c-ZrO_2 and $Ca_2Gd_8(SiO_4)_6O_2$ were found on the coating surface from 2 to 100 h, respectively. The T_m of CMAS powder is about 1250 °C,[9] indicating that CMAS melted and reacted with LGZ to produce $Ca_2Gd_8(SiO_4)_6O_2$. The $Ca_2Gd_8(SiO_4)_6O_2$ (apatite) and c-ZrO_2 peaks can also be confirmed in the same peaks after the high temperature reaction of Sc-doped $Gd_2Zr_2O_7$ and CMAS.[24] The peaks of c-ZrO_2 shift to higher angles with increasing exposure time. $Ca_2Gd_8(SiO_4)_6O_2$ is a phenomenon that occurs in the presence of CMAS. $Ca_2Gd_8(SiO_4)_6O_2$ shows a typical $P63/m$ (hexagonal) space group structure, which is similar to the XRD analysis result of 9.428 Å and the calculated lattice constant of 9.484 Å.[35] The space group of the c-ZrO_2 phase is Fm-$3m$ and the calculated lattice constant is 5.16 Å,[36] which is 5.11 Å similar to the XRD result. The a-axis constants of $Ca_2Gd_8(SiO_4)_6O_2$ and c-ZrO_2 are slightly smaller than the reference value. In another study, the calculated lattice constant of Yb^{3+}, Er^{3+}, Ho^{3+} and Tm^{3+} doped $Ca_2Gd_8(SiO_4)_6O_2$ (JCPDS card number 28-0212) was reported to be smaller than the experimental value of 9.421 Å, which is 9.484 Å. It was confirmed that the $Ca_2Gd_8(SiO_4)_6O_2$ lattice constant decreased after RE doping.[35] Apatite crystals are reported to be anisotropic in shape, oriented on average perpendicular to the surface and consistent with the [0001] axes trend.[37] The anisotropy could not be confirmed in this paper. However, the length and width of apatite were confirmed to have increased.

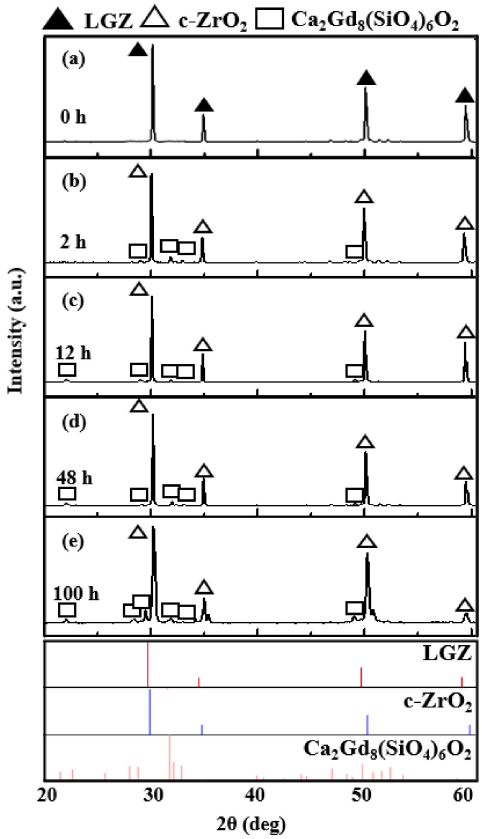

Fig. 1. XRD patterns of LGZ multilayer coatings exposed with CMAS to 1300 °C for (a) 0 h, (b) 2 h, (c) 12 h, (d) 48 h, and (e) 100 h.

3.2 High-temperature corrosion behavior

Figures 2(a) and 2(b) show the microstructure of LGZ before heat treatment. Figure 2(a) is the cross section of the coating. Figure 2(b) shows surface of the multilayer coating and micropores are observed. The total thickness of the coating layer is 550 µm. From the top position, LGZ (250 µm), LGZ + YSZ (150 µm), and YSZ (150 µm) layers are shown in Fig. 2(a). The results of EDS mapping analysis of the cross-sectional microstructure of the multilayer coating before exposure to CMAS in Fig. 2. As shown in Fig. 2(a), it is divided into LGZ, LGZ + YSZ, and YSZ layers from the top position. YSZ, which is mainly applied to TBC, is composed of the bottom layer, and LGZ + YSZ layer is composed to secure stability at high temperatures. In addition, LGZ on the top layer is the thickest layer for the high-temperature corrosion evaluation of CMAS. Figure 2(b) shows the surface of the coating and micropores can be identified. As seen in Fig. 2, Gd was prominent in the LGZ layer; Gd, Zr, and Y were prominent in the LGZ + YSZ layer; and the main components Zr and Y appeared prominently in the YSZ layer.

Figure 3 shows cross-sectional SEM micrographs of the microstructures of the multilayer coating layers exposed by CMAS at 1300 °C for (a) 2, (b) 12, (c) 48, and (d) 100 h. After heat treatment, the coating layer reacted with the molten CMAS to form a reaction layer. The reaction layer is composed of $Ca_2Gd_8(SiO_4)_6O_2$ and c-ZrO_2. In addition, the thickness of the reaction layer increased as the time of heat treatment increased. Consistent with the shown in Fig. 1, the formed reaction layer melted above

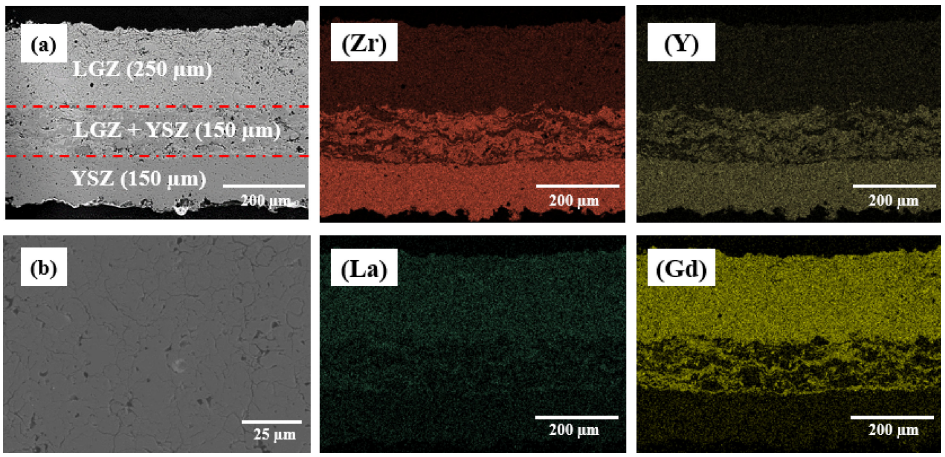

Fig. 2. SEM micrograph of (a) cross-sectional result with EDS maps of elements (Zr, Y, La, and Gd) and (b) surface of the multilayer coating.

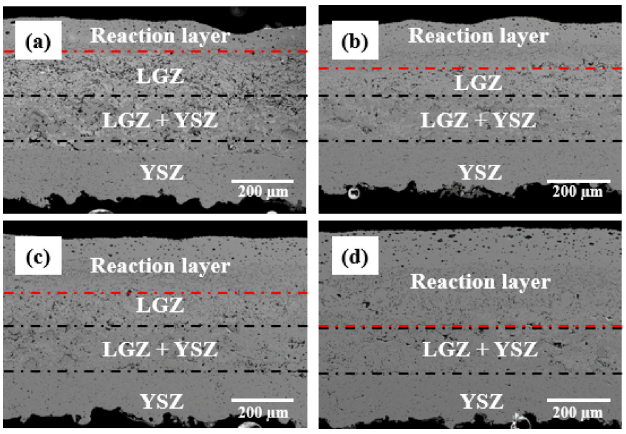

Fig. 3. Cross-sectional SEM micrograph of LGZ multilayer coatings that have interacted with CMAS at 1300 °C for (a) 2 h, (b) 12 h, (c) 48 h, and (d) 100 h.

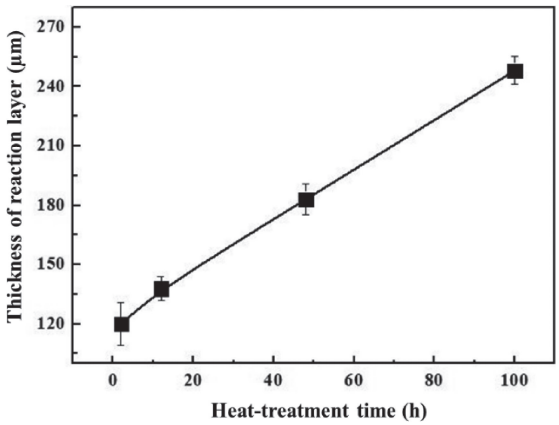

Fig. 4. Average thickness of reaction layer on LGZ multilayer coatings exposed to CMAS at 1300 °C as a function of heat-treatment time.

the T_m temperature of CMAS and reacted with LGZ, indicating that $Ca_2Gd_8(SiO_4)_6O_2$ was generated.

Figure 4 shows the thickness of the reaction layer according to the increase in reaction time after heat treatment at 1300 °C. The thickness of the reaction layer increased to about 118, 137, 185, and 253 μm after 2, 12, 48, and 100 h, respectively. After heat treatment, the CMAS and LGZ coating layers react rapidly, and the reaction layer formation rate is reduced. In our previous study, it was also confirmed that a reaction layer was quickly formed in the initial reaction, and the rate of reaction layer formation gradually decreased[12] from the results of the high-temperature corrosion behavior of CMAS and $Gd_2Si_2O_7$. Kramer et al.[38] fabricated columnar pyrochlore gadolinium zirconate TBC by EB-PVD and observed its corrosion resistance. The basic corrosion mechanism is that the reaction between rare earth zirconates and CMAS forms the $Ca_2Gd_8(SiO_4)_6O_2$ apatite phase. Consistent with the results of this study, the reaction between CMAS and zirconium gadolinium slows down after premature sealing of the channels in EB-PVD. It has been reported that this type of corrosion mechanism plays an important role in slowing down the CMAS attack on the coating, which is helpful for the survivability of the reaction layer during thermal cycling.[38] Another study fabricated three lanthanum zirconate TBCs designed with La/Zr ratios of 0.7:1 (LZO-7), 1:1 (LZO-10) and 2:1 (LZO-20).[39] As the amount of La increased, the content of the apatite phase increased, while the content of the fluorite phase decreased. It was concluded that among these lanthanum zirconate coatings, LZO-20 exhibited the best CMAS corrosion resistance. A dense and continuous layer of apatite $Ca_2La_8(SiO_4)_6O_2$ indicated that the subsequent infiltration of molten CMAS was effective.

Figure 5 shows the results of the EDS mapping analysis of a cross-section of the multilayer coating exposed by CMAS at 1300 °C for 2 h. The components detected in the EDS mapping component analysis were La, Gd, Ca, Si, Mg, Al, Zr, and Y. When comparing the depth of the reaction layer after high-temperature corrosion for the CMAS of $Gd_2Zr_2O_7$ and $La_2Zr_2O_7$, $La_2Zr_2O_7$ showed the formation of a deeper reaction layer.[40]

These results suggest that the reactivity between $La_2Zr_2O_7$ and the precipitate was higher than that of

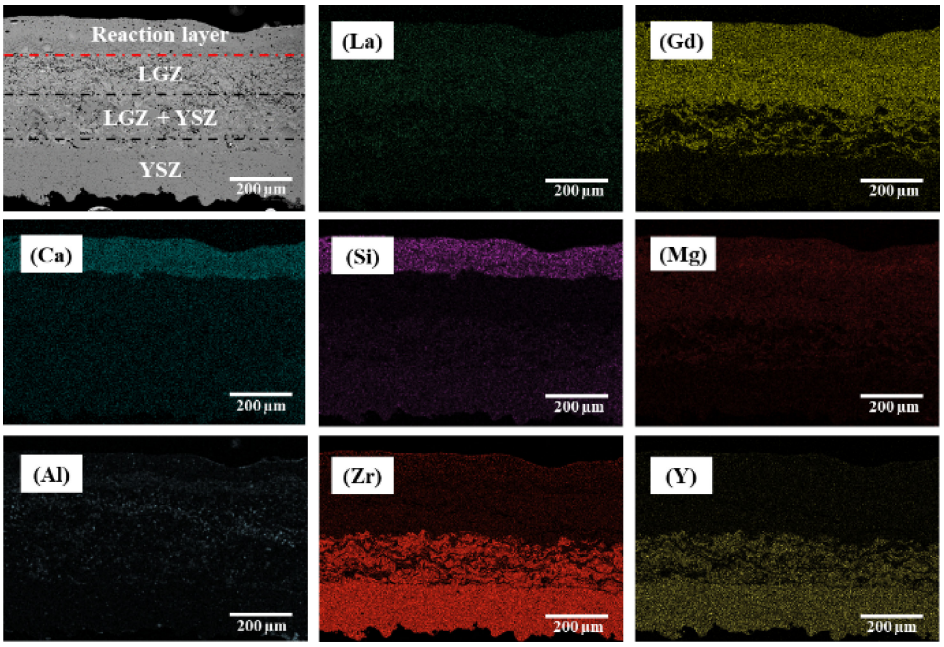

Fig. 5. Cross-sectional result with EDS maps of elements (La, Gd, Ca, Si, Mg, Al, Zr, and Y) of LGZ multilayer coatings that have interacted with CMAS at 1300 °C for 2 h.

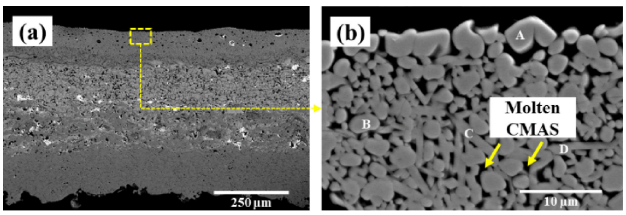

Fig. 6. (a) Low-magnification cross-sectional SEM micrograph of LGZ multilayer coatings after exposure to CMAS at 1300 °C for 2 h; (b) magnified view of region in yellow box of (a).

Table 1. The compositions (at.%) of the cross-section with CMAS for 2 h at parts A, B, C, and D shown in Fig. 6(b)

	Ca	Al	Si	Gd	Zr	La	O
A	1.8	0	0	5.5	32.1	1.3	59.3
B	1.6	0	0	6.8	34.5	1.5	55.6
C	7.1	2.0	17.9	21.2	1.3	1.8	48.7
D	8.9	2.2	18.6	21.4	1.9	2.0	45.0

$Gd_2Zr_2O_7$. In other words, the formation of a deeper reaction layer is expected with a cation radius of La (1.172 Å) larger than that of Gd (1.107 Å). We have studied the effect of the RE cation radius on the formation of the reaction layer previously.[9),10),12)] The formation of the reaction layer was lower with Er (1.004 Å) disilicate than with Gd (1.107 Å) disilicate. The reaction layer serves to fill pores, induce rapid densification, and prevent further infiltration of molten CMAS. It is desirable to form a reaction layer that can provide this protective function at a smaller thickness. In addition, reaction layer growth is dependent on several factors such as coating porosity, CMAS melt viscosity, temperature and time.

Figure 6(a) shows the SEM micrographs of the cross-section of the multilayer coating layer exposed by CMAS at 1300 °C for 2 h. Figure 6(b) is a high-magnification SEM micrograph of the yellow box in Fig. 6(a). The EDS point analysis results of A, B, C, and D shown in Fig. 6(b) are shown in **Table 1**. The reaction layer in Fig. 6(b) consists of sphere morphologies (points A and B) and needle morphologies (points C and D). In points A and B, mainly Zr, O and small amounts of Gd and La were detected. However, La, Gd, Ca, Si, and O were detected in points C and D. According to the XRD results (Fig. 1), points A and B are c-ZrO_2 fluorite dissolved in small amounts of Gd and La. Points C and D are also analyzed to be $Ca_2Gd_8(SiO_4)_6O_2$ apatite phase. $Ca_2La_8(SiO_4)_6O_2$ is formed through the reaction of $La_2Zr_2O_7$ and CMAS and forms a $Ca_2La_8(SiO_4)_6O_2$ to prevent further molten CMAS penetration.[26)] However, the small amount of La used in this study did not form a $Ca_2La_8(SiO_4)_6O_2$ after the CMAS reaction. It can be seen that a small amount of La is included in Table 1.

Figure 7 shows the results of EDS mapping analysis of a cross-section of the multilayer coating layer exposed by CMAS at 1300 °C for 100 h. La, Gd, Ca, Si, Mg, Al, Zr, and Y were analyzed using EDS mapping component analysis. As the high-temperature reaction time increased from 2 h (Fig. 5) to 100 h, changes in the reaction layer were confirmed through analysis of Ca and Si, the main components of apatite, the main phase of the reaction layer.

The reaction layer was slightly thicker as compared to at 2 h (Fig. 5), and about 170 μm was formed. As a result, it was confirmed that the reaction layer was quickly formed at the beginning of the reaction, but the rate of formation of the reaction layer slowed down as the time increased.

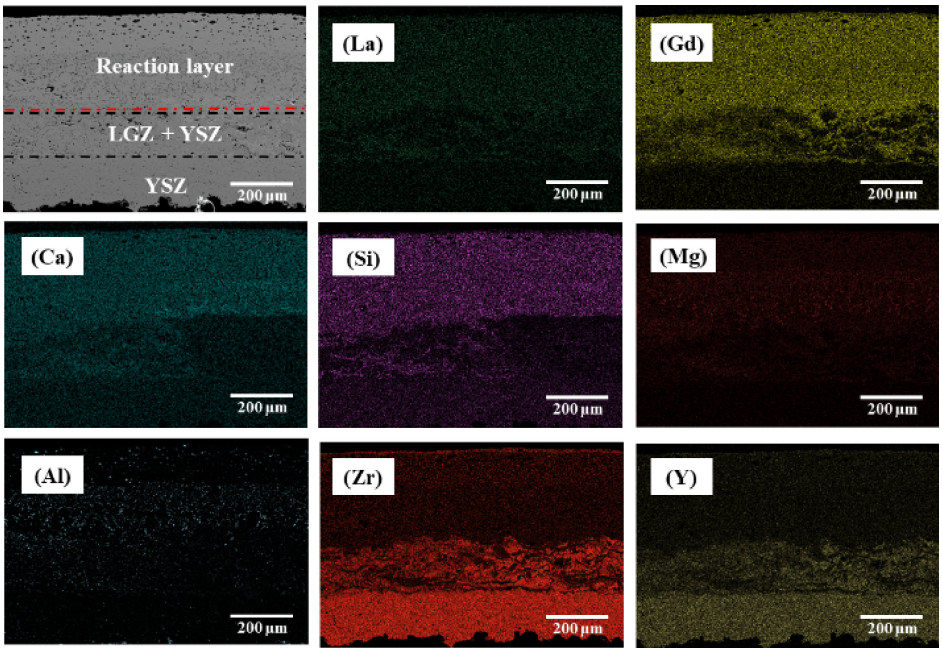

Fig. 7. Cross-sectional results with EDS maps of elements (La, Gd, Ca, Si, Mg, Al, Zr, and Y) of LGZ multilayer coatings that have interacted with CMAS at 1300 °C for 100 h.

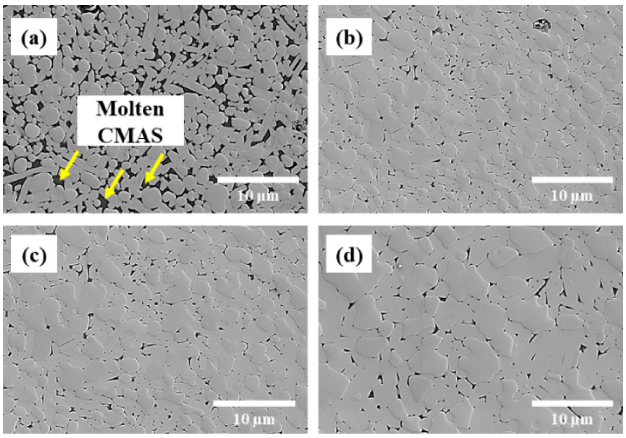

Fig. 8. Magnified view of a cross-sectional SEM micrograph of reaction layers that have interacted with CMAS at 1300 °C for (a) 2 h, (b) 12 h, (c) 48 h, and (d) 100 h.

Figure 8 shows the multilayer coating analysis exposed by CMAS at 1300 °C for (a) 2, (b) 12, (c) 48, and (d) 100 h. The reaction layer is composed of spherical c-ZrO_2 and needle morphology $Ca_2Gd_8(SiO_4)_6O_2$ apatite as shown in Fig. 6(b). It was confirmed that the sizes of c-ZrO_2 and apatite increased as the heat treatment time increased in Fig. 8(d). The increase in c-ZrO_2 and apatite size affects the densification of the coating and has a positive effect on the penetration of additional molten CMAS. Also, the porosity is sensitive to CMAS penetration at high temperatures, and a forming a more reactive generating layer is formed.[41),42)] Low porosity is good for corrosion resistance and leads to low reaction layer growth in coatings.[43)] Also, a major factor in the formation of the reaction layer is the reaction temperature. In particular, temperature affects the viscosity of the melt. The temperature and viscosity of molten CMAS were calculated using the VFT (Vogel Fulcher-Tammann) Eq. (3).[44)]

$$\log \eta = -4.55 + 7551/(T - 493) \quad (3)$$

Our previous study also evaluated the high-temperature corrosion behavior of CMAS melts according to temperature and viscosity.[10)] When the temperature increases, the viscosity decreases, and the penetration of the coating layer becomes easier. A reaction occurs between the molten CMAS and the coating layer, and the formation of a dense reaction layer prevents further penetration of the molten CMAS.

3.3 Mechanical properties

After heat treatment of the multilayer coating by CMAS at 1300 °C for various holding times, nanoindentation analysis was performed on the reaction layer, and the hardness and modulus of elasticity of the coating were measured.

As shown in **Figs. 9**(a) and 9(b), the hardness and Young's modulus before and after corrosion increased as the heat treatment time increased. The hardness before heat treatment (0 h) was 5.61 GPa and after 2 h, it was 6.78 GPa, an increase of about 20 %. After 12 h, the hardness increased to 7.76 GPa; after 48 h, the hardness increased to 8.14 GPa; and after 100 h, the hardness increased to 8.17 GPa in Fig. 9(a). The Young's modulus before heat treatment (0 h) was 113.5 GPa and increased to 169.9 GPa after 2 h. The hardness increased to 182.3 GPa after 12 h, to 185.5 GPa after 48 h, and to 186.2 GPa after 100 h in Fig. 9(b). It is confirmed that the hardness and Young's modulus are increased in the initial stage of corrosion reaction. The increase in the hardness of the coating after high-temperature corrosion is due to the reduction of pores

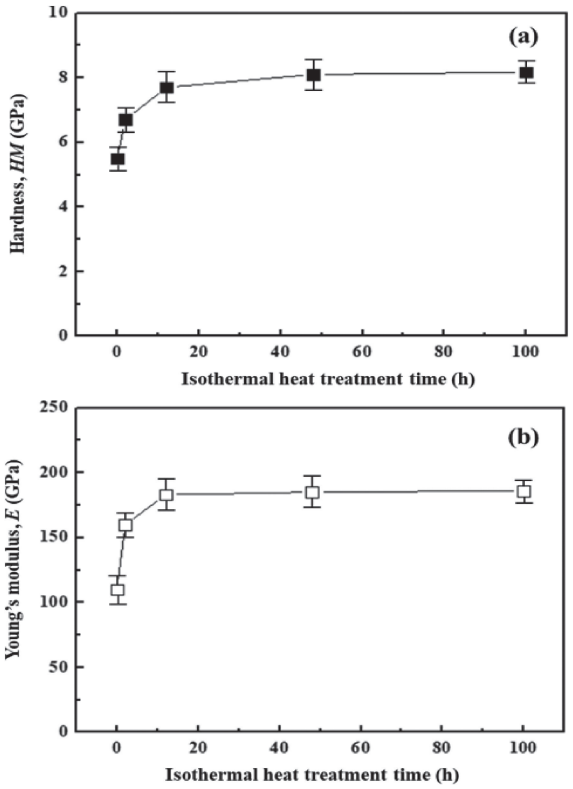

Fig. 9. (a) Martens hardness and (b) Young's moduli obtained from the reaction layer after heat treatment at 1300 °C.

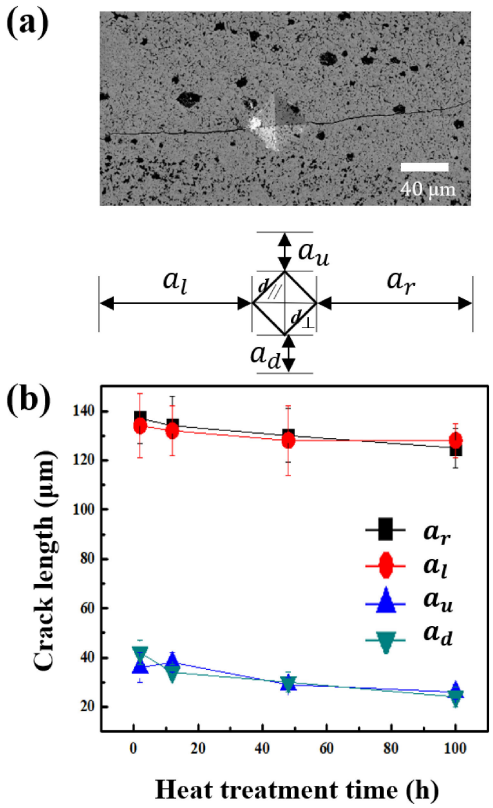

Fig. 10. (a) Microstructure of crack propagated by Vickers after heat treatment for 2 h. (b) Value of crack length according to heat treatment time.

in the coating through the penetration of molten CMAS, which affects densification. These results confirmed in our previous study that the hardness and Young's modulus of the EB-PVD coating side significantly decreased when the porosity increased.[25),29)] However, since the efficiency of TBCs is reduced due to high densification, appropriate improvement of TBCs according to the application environment is required. In addition, it was reported that high hardness for resistance to plastic deformation due to particle impact and low Young's modulus to avoid brittle fracture due to elastic deformation during initial impact have a positive effect on the erosion resistance of the coating system.[45)]

In addition, the coefficient of thermal expansion (CTE) of the resulting apatite ($10 \times 10^{-6}/K^{-1}$),[46)] $Gd_2Zr_2O_7$ ($10.4 \times 10^{-6}/K^{-1}$),[47)] and YSZ ($11 \times 10^{-6}/K^{-1}$),[47)] the mismatch between the bond coating ($15 \times 10^{-6}/K^{-1}$)[48)] and the CTE with the substrate causes an increase in residual stress, which increases the possibility of delamination of the coating. Thermal stress generated during cooling is one of the causes of top coating cracking.[49)] The resistance of a coating to low temperature impact induced cracking dt/dc can be expressed as Eq. (4).[50)]

$$\frac{dt}{dc} = \frac{1}{A}\left(\frac{K_{Ic}}{Y\sigma\sqrt{c}}\right)^n \propto \left(\frac{K_{Ic}}{E_c}\right)^n \quad (4)$$

where dt/dc is the crack growth rate; A is a constant and n is a value related to the properties of the material. K_{IC} is the coating fracture toughness. Y is the shape factor of the crack, σ is the thermal stress, and c is the crack length. Where E_c is the elastic modulus of the coating. K_{IC}/E_c reported that it would be a reasonable indicator to evaluate the mechanical resistance of coatings to impact.[50)] Cracking that occurs in actual operating environments has a significant impact on TBC lifespan. As a result of thermal cycling tests to determine the failure mechanism of LGZ/YSZ, vertical cracks mainly occurred in the YSZ layer because YSZ ($11.08 \times 10^{-6}/K^{-1}$) had a high TEC of LGZ ($10.33 \times 10^{-6}/K^{-1}$). Additionally, it was reported that horizontal cracks mainly occur at the interface of LGZ and YSZ.[51)] To evaluate the toughness, cracks were induced on the polished cross-section of specimens in reaction layer using a Vickers hardness indenter at a load of 0.5 kgf for 5 s. There are studies on the relationship between crack propagation behavior, microstructure and residual stress in coating layers.[34),52)–54)]

Figure 10(a) shows the microstructure of a crack propagated by Vickers after heat treatment for 2 h, and Fig. 10(b) shows the value of crack length according to heat treatment time. The induced cracks occurred in horizontal and vertical directions, with the "in-plane" and "through-the-thickness" directions defined as directions parallel and perpendicular direction, respectively. The crack length for the in-plane directions (a_r and a_l) was longer than that for the through-thickness directions (a_u and a_d). Since the crack was not affected by in-plane compressive stress, it tended to propagate in the in-plane direction.[34)]

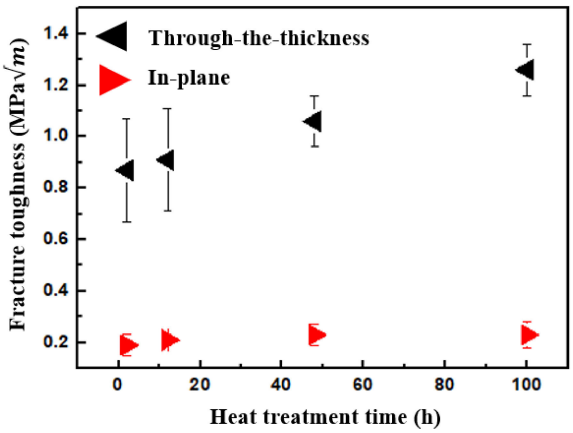

Fig. 11. Comparison of in-plane and through-thickness fracture toughness according to heat treatment time.

Figure 11 Comparison of in-plane and through-thickness fracture toughness according to heat treatment time. Fracture toughness slightly increased with heat treatment time in both directions.

This is due to the reduction of defects and splat boundaries, which can restrict crack propagation as sintering progresses.[34] The fracture toughness in the in-plane direction is 0.19–0.23 MPa$\sqrt{m}$. On the other hand, the fracture resistance in the thickness direction was 0.87–1.26 MPa$\sqrt{m}$, which was much higher than that in the in-plane direction. These results show that the crack eventually propagates in the in-plane direction and causes TBC delamination.

In summary, this study evaluated the high-temperature corrosion reaction layer of LGZ multilayer coating with CMAS, unlike the single-layer YSZ system applied to TBCs. In the initial stage of the corrosion reaction, the size of the needle morphology $Ca_2Gd_8(SiO_4)_6O_2$ phase and the reaction layer increased with time due to the penetration of molten CMAS. These results confirm that the hardness and Young's modulus are improved by preventing the penetration of additional molten CMAS through the densification of the coating. Therefore, the use of LGZ multilayer coating appears to constitute a promising strategy for designing TBCs.

4. Conclusions

The high-temperature corrosion behavior of candidate TBC material $(La,Gd)_2Zr_2O_7$/YSZ multilayer coating prepared by APS and exposed to CMAS was investigated for holding times of up to 100 h at 1300 °C. EDS analysis demonstrated that the coating layer was composed of LGZ, LGZ + YSZ, and YSZ layers from the top. In the initial stage of the high-temperature reaction, the thickness of the reaction layer was rapidly formed, and the reaction rate gradually decreased as time increased. Peaks corresponding to c-ZrO_2 and $Ca_2Gd_8(SiO_4)_6O_2$ were analyzed in the XRD results after heat treatment. These results indicate that molten CMAS reacted with LGZ to form $Ca_2Gd_8(SiO_4)_6O_2$. The reaction layer was composed of spherical morphology (c-ZrO_2) and needle morphology [$Ca_2Gd_8(SiO_4)_6O_2$] forms, as confirmed by SEM and EDS analysis. In addition, it was confirmed that in the initial stage of the corrosion reaction, the pores of the coating were reduced through the infiltration of molten CMAS, and the hardness and Young's modulus were greatly improved due to densification. The fracture toughness in the in-plane direction is 0.19–0.23 MPa$\sqrt{m}$. On the other hand, the fracture resistance in the thickness direction was 0.87–1.26 MPa$\sqrt{m}$, which was higher than that in the in-plane direction. These results show that the crack eventually propagates in the in-plane direction and causes TBC delamination. These results indicate that the LGZ multilayer coating layer will facilitate the development of TBCs with superior lifetime performance as compared to a single YSZ coating layer.

References

1) R. Vaßen, M. O. Jarligo, T. Steinke, D. E. Mack and D. Stover, *Surf. Coat. Tech.*, 205, 938–942 (2010).
2) K. S. Jang, E. Lee, T. W. Kim, I. S. Han, S. K. Woo and K. S. Lee, *J. Ceram. Soc. Jpn.*, 117, 582–587 (2009).
3) A. Vaidya, V. Srinivasan, T. Streibl, M. Friis, W. Chi and S. Sampath, *Mat. Sci. Eng. A-Struct.*, 497, 239–253 (2008).
4) Z. Wang, C. Zhou, H. Xu and S. Gong, *Chinese J. Aeronaut.*, 17, 119–123 (2004).
5) G. Pujol, F. Ansart, J. Bonino, A. Malie and S. Hamadi, *Surf. Coat. Tech.*, 237, 71–78 (2013).
6) S. H. Kim, T. Osada, Y. Matsushita, T. Hiroto, C. A. J. Fisher and B. K. Jang, *J. Eur. Ceram. Soc.*, 43, 6440–6448 (2023).
7) B. K. Jang, F. J. Feng, K. Suzuta, H. Tanaka, Y. Matsushita, K. S. Lee, S. Kim, Y. S. Oh and H.-T. Kim, *Ceram. Int.*, 43, 1880–1886 (2017).
8) B. K. Jang, F. J. Feng, K. Suzuta, H. Tanaka, Y. Matsushita, K. S. Lee and S. Ueno, *J. Ceram. Soc. Jpn.*, 125, 326–332 (2017).
9) S. H. Kim, C. A. J. Fisher, N. Nagashima, Y. Matsushita and B. K. Jang, *Ceram. Int.*, 48, 17369–17375 (2022).
10) S. H. Kim, N. Nagashima, Y. Matsushita, B. N. Kim and B. K. Jang, *J. Am. Ceram. Soc.*, 104, 3119–3129 (2021).
11) S. H. Kim, B. N. Kim, N. Nagashima, Y. Matsushita and B. K. Jang, *J. Eur. Ceram. Soc.*, 41, 3161–3166 (2021).
12) S. H. Kim, N. Nagashima, Y. Matsushita and B. K. Jang, *J. Eur. Ceram. Soc.*, 43, 593–599 (2023).
13) M. G. Gok and G. Goller, *J. Eur. Ceram. Soc.*, 36, 1755–1764 (2016).
14) E. Bakan, D. E. Mack, G. Mauer, R. Mucke and R. Vaßen, *J. Am. Ceram. Soc.*, 98, 2647–2654 (2015).
15) E. Sadri, F. Ashrafizadeh, A. Eslami, H. S. Jazi and H. Ehsaei, *Surf. Coat. Tech.*, 448, 128892 (2022).
16) Z. Y. Shen, L. M. He, R. D. Mu, Z. H. Xu and G. H. Huang, *Corros. Sci.*, 163, 108224 (2020).
17) Y. Ozgurluk, A. C. Karaoglanli and H. Ahlatci, *Vacuum*, 194, 110576 (2021).
18) D. Zhang, S. Gong, H. Xu and H. Guo, *Vacuum*, 70, 11–16 (2003).
19) B. K. Jang and H. Matsubara, *J. Alloy. Compd.*, 402, 237–241 (2005).
20) L. Wang, J. I. Eldridge and S. M. Guo, *Scripta Mater.*,

69, 674–677 (2013).
21) S. M. Naga, M. Awaad, H. F. El-Maghraby, A. M. Hassan, M. Elhoriny, A. Killinger and R. Gadow, *Mater. Design*, 102, 1–7 (2016).
22) K. S. Lee, D. H. Lee and T. W. Kim, *J. Ceram. Soc. Jpn.*, 122, 668–673 (2014).
23) B. Li, J. Wu, X. He, B. Wang and L. Guo, *Ceram. Int.*, 48, 11662–11671 (2022).
24) B. Li, J. Sun and L. Guo, *Corros. Sci.*, 193, 109899 (2021).
25) B. Liu, J. Y. Wang, Y. C. Zhou, T. Liao and F. Z. Li, *Acta Mater.*, 55, 2949–2957 (2007).
26) U. Schulz and W. Braue, *Surf. Coat. Tech.*, 235, 165–173 (2013).
27) B. K. Jang and H. Matsubara, *Mater. Lett.*, 59, 3462–3466 (2005).
28) W. C. Oliver and G. M. Pharr, *J. Mater. Res.*, 19, 3–20 (2004).
29) B. K. Jang, *J. Alloy. Compd.*, 426, 312–315 (2006).
30) B. K. Jang, F. J. Feng, K. S. Lee, E. García, A. Nistal, N. Nagashima, S. W. Kim, Y. S. Oh and H. T. Kim, *Surf. Coat. Tech.*, 308, 24–30 (2016).
31) B. K. Jang, S. H. Kim, C. A. J. Fisher and H. T. Kim, *Mater. Today Commun.*, 31, 103330 (2022).
32) S. H. Kim, C. A. J. Fisher, N. Nagashima, Y. Matsushita and B. K. Jang, *Ceram. Int.*, 49, 24268–24275 (2023).
33) B. K. Jang, N. Nagashima, S. W. Kim, Y. S. Oh, S. M. Lee and H. T. Kim, *J. Eur. Ceram. Soc.*, 40, 2667–2673 (2020).
34) Y. Arai, R. Inoue and H. Kakisawa, *Int. J. Appl. Ceram. Tec.*, 18, 947–956 (2021).
35) J. Zhang, G. Chen, Z. Zhai, H. Chen and Y. Zhang, *J. Alloy. Compd.*, 771, 838–846 (2019).
36) J. Ding, T. Tsuzuki and P. G. McCormick, *Nanostruct. Mater.*, 8, 75–81 (1997).
37) K. M. Grant, S. Kramer, G. G. E. Seward and C. G. Levi, *J. Am. Ceram. Soc.*, 93, 3504–3511 (2010).
38) S. Kramer, J. Yang and C. G. Levi, *J. Am. Ceram. Soc.*, 91, 576–583 (2008).
39) C. Zhu, Y. Liu, D. Wang, Y. Zhou, G. Yang, H. Chen, Y. Gao and B. Liu, *Ceram. Int.*, 44, 13908–13915 (2018).
40) U. Schulz and W. Braue, *Surf. Coat. Tech.*, 235, 165–173 (2013).
41) D. L. Poerschke, G. G. E. Seward and C. G. Levi, *J. Am. Ceram. Soc.*, 99, 651–659 (2016).
42) R. Naraparaju, R. P. Pubbysetty, P. Mechnich and U. Schulz, *J. Eur. Ceram. Soc.*, 38, 3333–3346 (2018).
43) S. Mahade, A. Venkat, N. Curry, M. Leitner and S. Joshi, *Coatings*, 11, 86–106 (2021).
44) D. Giordano, J. K. Russell and D. B. Dingwell, *Earth Planet. Sc. Lett.*, 271, 123–134 (2008).
45) S. Hassani, J. E. Klemberg-Sapieha, M. Bielawski, W. Beres, L. Martinu and M. Balazinski, *Wear*, 265, 879–887 (2008).
46) R. W. Jackson, E. M. Zaleski, B. T. Hazel, M. R. Begley and C. G. Levi, *Acta Mater.*, 132, 538–549 (2017).
47) M. G. Gok and G. Goller, "Intech Open", London, UK (2019).
48) R. Vaßen, F. Traeger and D. Stöver, *Int. J. Appl. Ceram. Tec.*, 1, 351–361 (2004).
49) C. G. Levi, J. W. Hutchinson, M. H. Vidal-Sétif and C. A. Johnson, *MRS Bull.*, 37, 932–941 (2012).
50) D. Zhou, D. E. Mack, E. Bakan, G. Mauer, D. Sebold, O. Guillon and R. Vaßen, *J. Am. Ceram. Soc.*, 103, 2048–2061 (2020).
51) Z. Shen, Z. Liu, R. Mu, L. He, G. Liu and Z. Huang, *Chem. Eng. J. Adv.*, 5, 100073 (2021).
52) H. Kakisawa and T. Nishimura, *Eur. Ceram. Soc.*, 38, 655–666 (2018).
53) H. Abe, K. Ikeda, H. Nakashima, F. Yoshida and K. Koga, *J. Ceram. Soc. Jpn.*, 108, 416–419 (2000).
54) K. Zeng and D. Rowcliffe, *J. Am. Ceram. Soc.*, 77, 524–530 (1994).